Soft Matter

ROYAL SOCIETY OF CHEMISTRY

PAPER

View Article Online
View Journal | View Issue

Cite this: *Soft Matter*, 2023, **19**, 7744

Finite elasticity of the vertex model and its role in rigidity of curved cellular tissues

Arthur Hernandez, *[a] Michael F. Staddon, [bcd] Michael Moshe [e] and M. Cristina Marchetti [a]

Received 4th July 2023,
Accepted 8th September 2023

DOI: 10.1039/d3sm00874f

rsc.li/soft-matter-journal

Using a mean field approach and simulations, we study the non-linear mechanical response of the vertex model (VM) of biological tissue to compression and dilation. The VM is known to exhibit a transition between solid and fluid-like, or floppy, states driven by geometric incompatibility. Target perimeter and area set a target shape which may not be geometrically achievable, thereby engendering frustration. Previously, an asymmetry in the linear elastic response was identified at the rigidity transition between compression and dilation. Here we show that the asymmetry extends away from the transition point for finite strains. Under finite compression, an initially solid VM can completely relax perimeter tension, resulting in a drop discontinuity in the mechanical response. Conversely, an initially floppy VM under dilation can rigidify and have a higher response. These observations imply that re-scaling of cell area shifts the transition between rigid and floppy states. Based on this insight, we calculate the re-scaling of cell area engendered by intrinsic curvature and write a prediction for the rigidity transition in the presence of curvature. The shift of the rigidity transition in the presence of curvature for the VM provides a new metric for predicting tissue rigidity from image data of curved tissues in a manner analogous to the flat case.

Understanding the emergence of form in organ development presents a major challenge to current continuum physics modeling of living systems. Unlike passive materials, biological tissues may tune their mechanical response to applied strains and forces by modifying cell shape and thereby be rigid or floppy. In particular, cell shape as characterized by the shape index $s \equiv \frac{P}{\sqrt{A}}$, with P and A the cell perimeter and area, has been found to serve as a metric for a solid–liquid transition at constant density in epithelial tissues.[1]

One widely studied model of epithelial tissues is the vertex model (VM) which describes the epithelium as a collection of vertices and edges in the 2D plane, reducing the tissue's structure to a polygonal tiling with possible edge tension. Unlike conventional spring network models which penalize deviations away from each edge length, the VM instead only sets a target cell area due to 3D bulk tissue incompressibility, along with terms capturing cell–cell edge adhesion and cell contractility,[2] which constrain the cell's perimeter. Thus the VM is less constrained than a spring network, *e.g.* crystalline solids, and naturally engenders zeros modes for any polygonal tiling.[2–4] Importantly, these zero modes exist at the level of a single cell. For example, assuming all cell edges have identical adhesion and contractility, the VM energy reduces to penalizing harmonic deviations away from a target area A_0 and target perimeter P_0. Thus in the VM each cell has 2 shape constraints, but a general polygon has at least 3 degrees of freedom such as is the case for triangles.[3]

Based on constraint counting it seems the VM can never support a solid state. Nonetheless the VM exhibits a rigidity transition between solid and floppy states tuned by the target shape index $s_0 = \frac{P_0}{\sqrt{A_0}}$ at a critical value s_0^*.[5] The transition is due to a geometric constraint set by the isoperimetric inequality which gives a lower bound on the ratio of $\frac{P}{\sqrt{A}}$ for n-gons admissible on the plane,[6]

$$\frac{P}{\sqrt{A}} \geq s_0^*(n), \tag{1}$$

where $s_0^* = \sqrt{4n\tan\left(\frac{\pi}{n}\right)}$ is the isoperimetric quotient. The lower bound sets an incompatible regime $\frac{P_0}{\sqrt{A_0}} < s_0^*$ where polygons cannot simultaneously achieve A_0 and P_0, and a compatible regime $\frac{P_0}{\sqrt{A_0}} \geq s_0^*$ where polygons may achieve both A_0 and P_0. This geometric constraint on shape indicates that rigidity stems from self-tension due to geometrical incompatibility.

[a] *Department of Physics, University of California Santa Barbara, Santa Barbara, CA 93106, USA. E-mail: arthurhernandez@ucsb.edu*
[b] *Center for Systems Biology Dresden, Dresden, Germany*
[c] *Max Planck Institute for the Physics of Complex Systems, Dresden, Germany*
[d] *Max Planck Institute of Molecular Cell Biology and Genetics, Dresden, Germany*
[e] *Racah Institute of Physics, The Hebrew University of Jerusalem, 91904, Jerusalem, Israel*

For VM simulations consisting of ordered tilings (triangles, squares, hexagons) in the plane the rigidity transition occurs exactly at $s_0^*(n)$.[3,7] In simulations of disordered VMs the transition occurs at approximately $s_0^*(5) \simeq 3.81$.[5]

The linear response of the VM to mechanical deformations is well studied,[3,8–10] but the non-linear response relatively less so. Recent work showed that the VM exhibits shear-thickening in the compatible regime.[4,11] In the same vein, our work presents a careful study of the non-linear elasticity of the VM under finite dilation and compression *via* a mean-field approach and simulations. In previous work by the authors, the onset of compatibility in the VM at s_0^* showed anomalous elasticity as reflected by an asymmetric bulk modulus under dilation and compression, as well as coupling between stretching and shear modes.[3] In this article, we show that the asymmetry of the bulk modulus extends away from s_0^* under finite compression and dilation. In particular, the VM exhibits a dilation-hardening for compatible tissues and a compression-softening of incompatible tissues for finite critical strain. The hardening (softening) nonlinear response to dilation (compression) is reflected by a jump (drop) discontinuity of the bulk modulus and is associated with the sudden lifting (onset) of zero-modes.

These results are of particular importance to systems that are residually stressed, such as cell layers with spatially varying cell geometry or curved tissue, where they may result in a shift of the critical s_0^*. In general, understanding the mechanisms through which tissues fine-tune their rigidity in response to areal re-scaling is relevant to several biological processes, such as tissue growth, shrinkage, response to applied deformations, and in particular to shape changes where 2D tissue layers spontaneously fold into 3D curved states.[12–14] Based on insight from the planar 2D non-linear elasticity, we use mean field theory to predict how local compression/dilation due to intrinsic curvature shifts the transition between rigid and floppy states in curved tissue.

The organization of the paper is as follows: in Section 1 we introduce our mean-field VM, which describes 2D tissue elasticity at the single cell level. Section 2 outlines the calculation of the non-linear bulk modulus of the mean-field model and discusses simulation results. In Section 3 we give a description of complementary numerical methods used to test our mean field theory. In Section 4 we present a Landau energy argument to elucidate the connection between the asymmetry of the bulk modulus and the finite critical strain that controls the onset/lifting of zero-modes. Section 5 uses our results from mean field theory to predict the effective critical shape index for cells on a curved surface. We show that our prediction for the rigidity transition in curved geometry agrees well with numerical simulations by Sussman.[15] We conclude with a brief discussion in Section 6.

1 Mean-field theory of ordered vertex model

Our mean field theory considers a uniform regular 2D tiling where all cells respond identically to applied deformations. This approximation can capture the response of tissues subjected to uniform constraints or loads. The tissue energy is the sum of the energies of identical individual cells, and therefore our mean field approach reduces the VM to a single polygonal cell. All bulk tissue properties, such as elastic moduli, are calculated at the single cell level. Details of the mean field model are given in Appendix A.3, and a thorough study by the authors is in ref. 3. The simulations are carried out for a lattice of regular polygons. For concreteness, our simulations and mean field theory are for hexagonal cells unless stated otherwise. All results hold analogously for other polygons.

Lengths are rescaled by $\sqrt{A_0}$ and the tissue energy per cell is rescaled by $\kappa_A {A_0}^2$, with κ_A the area stiffness, such that the energy per cell contains only two dimensionless free parameters and is given by

$$E = \frac{1}{2}(a-1)^2 + \frac{r}{2}(p-s_0)^2, \tag{2}$$

where $r \equiv \frac{\kappa_P}{\kappa_A A_0}$ is the rigidity ratio, $s_0 \equiv \frac{P_0}{\sqrt{A_0}}$ the target shape index, and a and p are the actual area and perimeter of the cell.

To parameterize cell shape degrees of freedom, we work with a Cartesian coordinate system (X,Y) encompassing the cell with Y along the height, and X along the width, as shown in Fig. 1. The area and perimeter of a cell are purely geometric objects, and shape changes under various deformations can be computed given a transformation law.

Externally imposed dilation and compression are implemented *via* an overall re-scaling of the cell's height h and width w *via* the transformation

$$w \to w(1+\epsilon), \tag{3}$$

$$h \to h(1+\epsilon), \tag{4}$$

with $\epsilon \in (-1, 1)$. In response to the strain, the cell may also spontaneously shear while maintaining the imposed rescaled area, as shown in Fig. 1. This "tilt" is a self-shear parameterized as

$$w \to w + th, \tag{5}$$

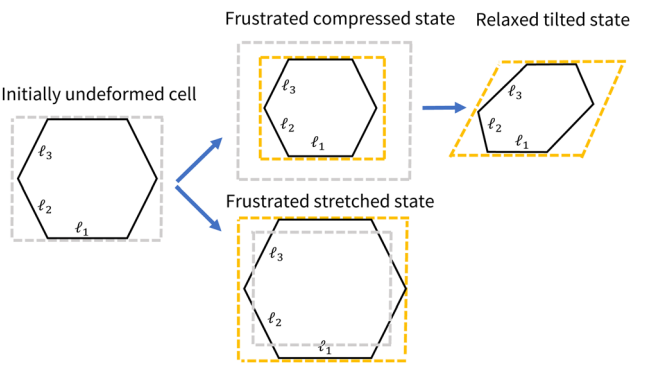

Fig. 1 Under compression/dilation a cell may respond *via* a self-shear transformation by tilting either right or left. For example, at the rigidity transition, $s_0 = s_0^*$, both compression and dilation induce perimeter and area tension. Only under compression, however, cells can relax perimeter tension by changing shape, while simultaneously preserving area.

$$h \to h, \tag{6}$$

where $t(\theta) \equiv \tan(\theta)$ parametrizes the shape degeneracy of cells. In addition, hexagonal cells can also respond *via* non-affine deformations, which are known to reduce the shear and Young's moduli in the incompatible regime.[16] In this study we preclude non-affine pathways for cell response as our previous work showed this approximation captures well the response to isotropic compression/dilation.[3]

The deformed energy of an isotropically dilated or compressed cell is then given by

$$E(\epsilon, \theta; s_0, r) = \frac{1}{2}\left[\ell^2(1+\epsilon)^2 - 1\right]^2 + \frac{r}{2}\left[p(\epsilon, \theta, \ell) - s_0\right]^2, \tag{7}$$

where $\ell(s_0,r)$ is the rescaled undeformed characteristic cell size (see Appendix A.3 for details) and the deformed perimeter is

$$p(\epsilon, \theta, \ell) = \frac{\sqrt{2}\ell}{3^{3/4}}(1+\epsilon)\left(2\sqrt{1+t(\theta)^2} + \sqrt{1+(t(\theta)-\sqrt{3})^2} + \sqrt{1+\left(t(\theta)+\sqrt{3}\right)^2}\right). \tag{8}$$

If we set $\epsilon = 0$ and minimize with respect to θ we recover the results of ref. 3: the ground state energy is gapped for $s_0 < s_0^*$ and vanishes for $s_0 \geq s_0^*$, with a manifold of degenerate shapes, or zero-modes, parametrized by θ. To study the response to $\epsilon \neq 0$ we minimize θ as a function of applied strain in a manner analogous to our study of the linear response.[3] Formally, the energetic response is given by

$$E = \min_{\theta} E(\epsilon, \theta; s_0, r). \tag{9}$$

Because height and width are fixed by dilation/compression the energy minimization is 1D and corresponds to solving,

$$\left.\frac{\partial E}{\partial \theta}\right|_{s,r,\epsilon} = (p - s_0)\left.\frac{\partial p}{\partial \theta}\right|_{s_0,r,\epsilon} = 0. \tag{10}$$

This equation has two solutions: either a cell utilizes shape degeneracy *via* θ so that the perimeter accommodates both dilation/compression and target shape index s_0, or the perimeter is totally set by dilation/compression with no tilt response. The relevant energy minimizing solution is a function of s_0, r and ϵ.

2 Nonlinear elasticity

The non-linear response under finite dilation and compression is characterized by the bulk modulus, defined as

$$K = \frac{1}{2a_{\text{cell}}}\left(\frac{\partial^2}{\partial \varepsilon^2}\min_{\theta_{\min}} E(\epsilon, \theta; s_0, r)\right)_{s_0,r,\epsilon} \tag{11}$$

where $a_{\text{cell}} = \frac{3\sqrt{3}}{2}\ell^2$ is the rescaled cell area. Evaluating eqn (11) at $\epsilon = 0$ yields the linear response, whereas a finite ϵ gives the non-linear response under finite strains. The minimization with respect to θ must be carried out before differentiation because the self-shear is implicitly dependent on ε *via* eqn (10).

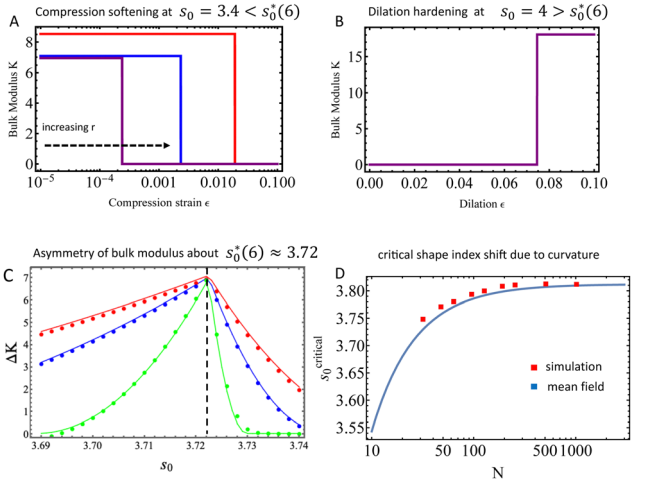

Fig. 2 Panel A shows the mean field non-linear bulk modulus *versus* compressive strain in the incompatible regime for r = 1, 10, 100. A sudden discontinuous softening occurs at a critical strain ϵ_*. Panel B shows the hardening of the mean field bulk modulus at a critical dilation in the compatible regime. Note that in the incompatible regime ϵ_* depends on r and is thereby sensitive to the balance between perimeter and areal elasticity, whereas in the compatible regime, the critical strain is only a function of the shape index. Panel C compares the mean field model (solid line) to simulation (dots) and shows the difference in the linear response between dilation and compression for strain magnitudes ε = |0.01|, |0.006|, |0.002| in red, blue and green, respectively. The asymmetry of the response decays continuously away from the critical shape index. Panels A, B, and C corresponds to hexagons. Panel D shows the effective critical shape index for a random tiling of N cells on a sphere of radius $R_g = \sqrt{\frac{N}{4\pi}}$. The mean field prediction is for pentagons, whereas the simulation data are for a disordered VM taken from ref. 15.

In the incompatible solid state, $(s_0 < s_0^*)$, we find that the mean field model and simulations exhibit a discontinuous drop in the bulk modulus at a critical compression. The discontinuity occurs due to a spontaneous self-shear of the cell which allows the perimeter tension to vanish. Conversely, under dilation the bulk modulus remains continuous as a function of strain, as shown in Fig. 2(A). Increasing r shifts the critical strain to higher values, reflecting how a higher perimeter tension may support higher compression before giving way to spontaneous self-shear.

In the compatible floppy state, $(s_0 > s_0^*)$, the bulk modulus is continuous under any finite compression but exhibits a discontinuous jump at a critical strain upon dilation, as shown in Fig. 2(B). At sufficient dilation, the zero-modes of the degenerate ground state are "exhausted", resulting in a frustrated and thereby rigid state. Unlike the incompatible state, the critical dilation is insensitive to r.

At the transition, s_0^*, both dilation hardening and compression softening are present for arbitrarily small strains, and reflect an asymmetry of the response to area rescaling. To quantify the asymmetry of the response, we show in Fig. 2(C) the difference between dilation and compression bulk modulus ΔK as a function of s_0 for various values of the dilation/compression strain. For s_0 near the critical value, s_0^*, the

asymmetry persists away from the critical point even for modest values of the strain (>0.002). Note that the curve ΔK *vs.* s_0 is also not symmetric about the $s_0 = s_0^*$ axis; this is due to the fact that the critical strain depends on r in the incompatible state, but not in the compatible state.

The origin of the bulk modulus discontinuity can be in part understood by writing the explicit expression for K obtained from eqn (11)

$$K = \frac{1}{2a_{\text{cell}}}\left[a^2 + r[p(\theta_{\min}) - s_0]\frac{\partial^2 p(\theta_{\min})}{\partial \varepsilon^2} + r\left(\frac{\partial p(\theta_{\min})}{\partial \varepsilon}\right)^2\right]. \tag{12}$$

The contribution due to perimeter tension, $r(p(\theta_{\min}) - s_0)$, in the solid phase vanishes if cells can accommodate target perimeter and imposed compression simultaneously *via* self-shear, resulting in a discontinuous drop of the bulk modulus. Conversely, in the floppy phase sufficient dilation will result in a sudden contribution from perimeter tension. In the following section, we formulate a Landau-type energy analysis to understand how dilation/compression can trigger or suppress zero-modes associated with shape deformation under dilation and compression.

3 Simulation protocol

We perform numerical simulations of the deformation protocol in the incompatible regime $\left(s_0 < s_0^*(6)\right)$ using a tissue of 4 hexagonal cells in a periodic box of lengths L_x and L_y. We use regular hexagons with $l_1 = l_2 = l_3$ determined by energy minimization. This also determines the periodic box lengths. We apply a strain of size ε by mapping all vertex positions $x \to x(1+\varepsilon)$ and $y \to y(1+\varepsilon)$ and the box $L_x \to L_x(1+\varepsilon)$, $L_y \to L_y(1+\varepsilon)$. We then minimize energy with respect to the vertex positions with the new box size. We measure the bulk modulus as $K = \frac{1}{L_x L_y}\frac{2\delta E}{\varepsilon}$, where δE is the change in minimum energy before and after strain. The simulations were performed with the Surface Evolver software.[17]

4 Landau energy expansion

To understand how compression or dilation may trigger or lift shape degeneracy we treat θ as an order parameter for the onset of shape degeneracy. In other words, a finite θ signals that cells can adjust their shape to accommodate imposed strains, while $\theta = 0$ when cells remain rigid and do not change shape in response to external strain.

We expand the energy given by eqn (7) in power of θ to quartic order,

$$E(\epsilon, \theta; s_0, r) = E(\epsilon, s_0, r) + \frac{\alpha}{2}\theta^2 + \frac{\beta}{4}\theta^4 + \mathcal{O}(\theta^6), \tag{13}$$

where

$$\alpha = 3\sqrt{3} r \ell_\epsilon \left(\ell_\epsilon - \frac{s_0}{s_0^*(6)}\right), \tag{14}$$

$$\beta = \frac{107\sqrt{3}}{32} r \ell_\epsilon \left(\ell_\epsilon - \frac{89}{107}\frac{s_0}{s_0^*(6)}\right), \tag{15}$$

and $\ell_\epsilon \equiv \ell(1+\epsilon)$. Minimization of this approximate θ^4 energy gives two solutions: (i) $\theta_{\min} = 0$ for $\alpha > 0$, and (ii) $\theta_{\min} = \pm\sqrt{\frac{|\alpha|}{\beta}}$ for $\alpha < 0$. The Landau expansion highlights the role of strain ε as tuning parameter between the cell responding with $\theta_{\min} = 0$ or by spontaneously tilting *via* a shear of $\theta_{\min} = \pm\sqrt{\frac{|\alpha|}{\beta}}$. The form of α reflects an asymmetric response between compression *versus* dilation. From α we can extract the critical strain, ϵ_*, which controls the onset/lifting of shape degeneracy.

$$\epsilon_* = \frac{1}{\ell}\frac{s_0}{s_0^*(6)} - 1 \tag{16}$$

The vanishing of the critical strain at the critical shape index coincides with the failure of linear elasticity for any applied strain.[3] Note that our expansion implies a tricritical point. Specifically, $\beta < 0$ occurs around the transition point $s_0 \approx 3.72$ either for large compression of $\varepsilon \approx -0.17$, or for smaller strains deep in the floppy/compatible regime, around $s_0 \approx 4.47$. However, our Landau expansion only considers a single pathway, *via* θ, by which cells may respond to moderately imposed strains. To handle larger deformations we would need to increase the expansion and/or incorporate other affine and non-affine pathways of cell-level response. Thus we take $\beta > 0$ to define the limits for which our expansion is valid.

In the compatible regime $\ell = 1$ because target area is always achieved and ϵ_* is independent of the rigidity ratio r. Whereas in the incompatible regime ϵ_* depends on r through ℓ.

We input the cell response *via* $\theta_{\min}$ into the energy and expand in powers of strain ε.

$$E(\epsilon; s_0, r) = \min_\theta E(\epsilon, \theta; s_0, r) \tag{17}$$

$$= \min_\theta E(\epsilon, s_0, r) + \frac{\alpha}{2}\theta^2 + \frac{\beta}{4}\theta^4 + \mathcal{O}(\theta^5, \epsilon^3) \tag{18}$$

$$= E_0 + \frac{1}{2}\left(\frac{\partial^2 E(\theta_{\min})}{\partial^2 \epsilon}\right)\varepsilon^2 + \mathcal{O}(\epsilon^3). \tag{19}$$

In the final line the harmonic coefficient contains contributions from θ which reduce the overall response of the tissue. If we do not minimize over θ before expanding in ϵ, the resultant deformed energy does not incorporate the self-shear response due to cell shape changes. A summary of the consequences of the additional degree of freedom θ on the response are as follows: in the incompatible regime, the $\theta_{\min} = 0$ solution corresponds to a linear response in the solid state (see Fig. 4), whereas $\theta_{\min} = \pm\sqrt{\frac{|\alpha|}{\beta}}$ corresponds to the softer renormalized nonlinear response at critical compression strain. On the other hand, in the compatible regime, the linear response is

always given by $\theta_{\min} = \pm\sqrt{\frac{|\alpha|}{\beta}}$ which allows the perimeter tension to vanish. The hardening under finite dilation occurs at a critical dilative strain ϵ_* and corresponds to a switch from $\theta_{\min} = \pm\sqrt{\frac{|\alpha|}{\beta}}$ to $\theta_{\min} = 0$, resulting in a higher response. This hardening phenomena is due to the cell's inability to access degenerate ground states to accommodate large dilation.

4.1 Strain dependent critical shape index

So far our mean-field model has predicted how compression (dilation) controls the onset (lifting) of shape degeneracy. The rigidity of the solid is defined by the absence of zero modes at the single-cell level. Therefore the mean field treatment suggests that dilation and compression shift the rigidity transition of the VM.

The shifted critical shape index is determined by the condition $\alpha(s_0, \epsilon) = 0$. Solving for s_0 yields a simple linear relationship between the effective critical point and strain

$$s_0^{\text{critical}} = s_0^*(n)\ell(1+\varepsilon), \tag{20}$$

where we used the modified version of eqn (14) for n-gons (see Appendix A.3). Note that the absence of rigidity does not mean absence of residual stresses, as area tension is still finite. This is reminiscent of the simultaneous existence of zero-modes and states of self stress,[18] as well as the simultaneous onset of soft modes and geometric frustration.[19,20] From eqn (20) we construct a phase diagram in Fig. 3 showing how both tuning target shape index and imposed areal strain can control the onset of rigidity.

So far we discussed the effect of finite strains on the value of the effective critical shape parameter, regardless of the origin of strain. One possible source of strain that is highly relevant to biological tissue is curvature, as is the case in bronchial epithelial tissue and early stage embryos.[12] A simple toy model to understand the effect of curvature is a two-dimensional spherical tissue model. The sphere radius may induce effective tension or compression on cells depending on their total preferred area which may be smaller or larger than $4\pi R^2$.

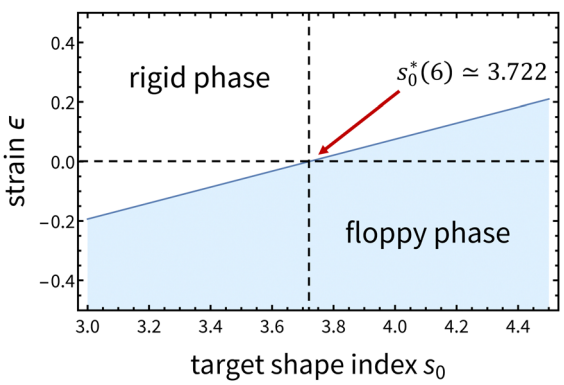

Fig. 3 Phase diagram detailing how both target shape index and imposed compression/dilation control the floppy-rigid transition for hexagons as described by eqn (20) for rigidity ratio $r \gg 1$.

Simulations of the VM constrained on a sphere have in fact reported that the rigidity transition signaled by the critical target shape index is sensitive to curvature with s_0^* shifts depending on curvature magnitude and relative cell size.[15]

In the rest of this article, we examine the effective dilation/compression induced by curvature by calculating the cell area on a curved surface relative to its flat counterpart. Utilizing eqn (20), we then predict the critical target shape index for solid–liquid transition of curved 2D tissues.

5 Rigidity transition in the presence of curvature

We extend the mean field treatment by perturbatively calculating cell area on surfaces of constant curvature in powers of $\mathcal{G}R_{\text{cell}}{}^2$, where $\mathcal{G}$ is the Gaussian curvature, and R_{cell} the cell radius. Regular polygons of fixed radius (defined as the distance of the centroid to a vertex) differ in area depending on the surface on which they are embedded. The mismatch in area between curved and flat cells engenders an effective strain.

All geometric information of a surface M is encoded in the metric tensor $\mathbf{g}$. For a general shape/cell on a surface, $D \subset M$, the area is defined as

$$A = \int_D \sqrt{\det g}\, \mathrm{d}^2x \tag{21}$$

The determinant of the metric serves as a weight which accounts for the local compression/dilation between points. Unlike the planar setting of the mean field model where $g_{ij} = \delta_{ij}$, the metric on curved surfaces – even uniformly curved – is not homogeneous but a function of space. Nonetheless, the metric always admits a local expansion in *normal coordinates*, (x_0, x^i) which are defined by the condition that geodesics can be locally parameterized as straight lines, *i.e.* $\gamma(\lambda) = (x^1\lambda, x^2\lambda)$. In these coordinates, a series expansion of the metric in powers of curvature yields

$$\det(g) = 1 - \frac{\mathcal{G}}{3}|x|^2 + \mathcal{O}(|x|^3). \tag{22}$$

The expansion reflects how variations of the metric are tied to curvature, and is locally approximated as flat with higher order corrections. The derivation of eqn (22) is given in Appendix A.1.

In our calculation we restrict attention to surfaces of uniform curvature – constant $\mathcal{G}$ – and hence we only consider flat, spherical, and saddle-like surfaces. Of course, real curved biological tissues are not uniform either due to boundary conditions or heterogeneities. Our approximation is controlled by the dimensionless geometric parameter η set by the radius R_{cell} of the cell over the radius of curvature $R_{\mathcal{G}}$, $\eta \equiv \frac{R_{\text{cell}}}{|R_{\mathcal{G}}|}$, where $\mathcal{G} \equiv \pm\frac{1}{R_{\mathcal{G}}{}^2}$. Our mean field result will hold best for tissues with moderate curvature or relativity small cells.

5.1 Area of cells on curved surfaces

Upon series expansion of the metric, the area to quadratic order is given by,

$$\begin{aligned} A &= \int_D \sqrt{\det g}\,\mathrm{d}^2x \\ &\approx \int_D \mathrm{d}^2x - \frac{\mathcal{G}}{6}\int_D |x|^2\mathrm{d}^2x, \end{aligned} \tag{23}$$

The first term yields the flat area. We generalize our calculation to n-sided polygons for easy comparison of various tilings. To parameterize the polygonal n-sided cell D we decompose it into $2n$ triangles about the centroid as illustrated in Fig. 4. Details are given in Appendix A.2. To quadratic order the area is

$$A = \bar{A}\left(1 - \frac{\mathcal{G}}{12}{R_{\mathrm{cell}}}^2 f(n) + \mathcal{O}\left({R_{\mathrm{cell}}}^4\right)\right), \tag{24}$$

where $\bar{A} = n{R_{\mathrm{cell}}}^2 \cos\left(\frac{\pi}{n}\right)^2 \tan\left(\frac{\pi}{n}\right)$ is the flat area of the cell, and $f(n) \equiv \cos^2\left(\frac{\pi}{n}\right)\left(\frac{2}{3} + \frac{1}{3}\sec^2\left(\frac{\pi}{n}\right)\right)$. In the limit of either very small cell size or very small curvature, the area reduces to the flat case. In the limit $n \to \infty$ the first correction yields $\frac{\mathcal{G}}{12}\pi{R_{\mathrm{cell}}}^2$, which reproduces the classical result of Bertand–Diguet–Puiseux on the area comparison of 2D geodesic balls of radius R_{cell} between curved and flat spaces.[21]

5.2 Shift of the rigidity transition

From eqn (24) and the form of the deformed area term in eqn (7) we may write the induced dilation/compression strain set by curvature as

$$\begin{aligned} \varepsilon_{\mathcal{R}}(n) &= -1 + \sqrt{1 - \frac{\mathcal{G}}{12}{R_{\mathrm{cell}}}^2 f(n)} \\ &= -1 + \sqrt{1 - \cos^2\left(\frac{\pi}{n}\right)\left(\frac{2}{3} + \frac{1}{3}\sec^2\left(\frac{\pi}{n}\right)\right)\frac{\mathcal{G}}{12}{R_{\mathrm{cell}}}^2}. \end{aligned} \tag{25}$$

The effective strain depends on the number of edges due to the discrete rotational symmetry of polygons: points on each edge are weighted according to their distance from the centroid. The predicted shift in the critical shape index is

$$\begin{aligned} s_0^{\mathrm{critical}}(n,\mathcal{G}) &= s_0^*(n)\ell(n)(1+\epsilon_{\mathcal{G}}(n)) \\ &\approx s_0^*(n)(1+\epsilon_{\mathcal{G}}(n)) \end{aligned} \tag{26}$$

where we have set $\ell \approx 1$, which restricts our prediction near the planar critical target shape index or large rigidity ratio $r \gg 1$.

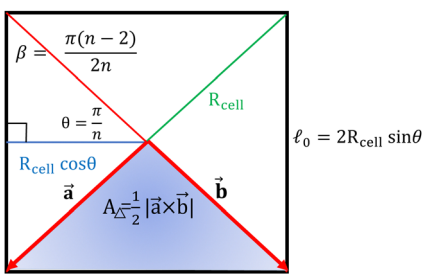

Fig. 4 The shape of a regular polygon can be determined by the number of edges and the length of each edge. To modify and aide our calculation for various n-gons, we decompose a polygon into n triangular wedges as illustrated in the figure. Thus one may specify a regular polygon by the number edges and either the edge length ℓ_0 or cell radius R_{cell}.

5.3 Comparison with simulation

In recent work by Sussman[15] a disordered vertex model of N cells on a uniform sphere of radius $R_{\mathcal{G}} = \sqrt{\frac{N}{4\pi}}$ was simulated for various N. At the onset of rigidity the critical shape index was extracted and reported to vary as a function of N, which monotonically increased until plateauing at $s_0^*(5) \sim 3.812$ for large N (see Fig. 2(D)).

To compare with simulation[15] we re-cast $\mathcal{G}{R_{\mathrm{cell}}}^2$ in terms of N and consider the mean field treatment for pentagons, $n = 5$, corresponding to the rigidity of a disordered VM in the flat case. Sussman considered a sphere of radius $R_{\mathcal{G}} = \sqrt{\frac{N}{4\pi}}$ with average cell area set to unity, *i.e.* $A_{\mathrm{cell}} \equiv \frac{N}{4\pi L^2} = 1$. Our mean field calculation is for a single cell and so we take R_{cell} corresponding to a pentagon. Thus $5{R_{\mathrm{cell}}}^2 \cos\left(\frac{\pi}{5}\right)^2 \tan\left(\frac{\pi}{5}\right) = 1 \Rightarrow {R_{\mathrm{cell}}}^2 \approx \frac{1}{2.377}$ (see eqn (40)).

Therefore the relative ratio of cell size to radius of curvature goes as $\frac{{R_{\mathrm{cell}}}^2}{{R_{\mathcal{G}}}^2} \approx \frac{4\pi}{2.377}\frac{1}{N}$. This yields the predicted critical shape index

$$s_0^{\mathrm{critical}}(n=5,N) \approx 3.812\left(1 - \frac{1.36}{N}\right)^{1/2}. \tag{27}$$

A comparison of our results to the simulations of ref. 15 is shown in Fig. 2(D).

Besides expanding to higher order, the calculation can be improved by computing the ground state characteristic cell size ℓ_0 for curved vertex models, but this is beyond our mean field approach. Additionally,[15] reports that the shape index distribution broadens for larger ${R_{\mathrm{cell}}}^2\mathcal{G}$ (smaller N) reflecting a greater diversity of polygons at the rigidity transition than the flat counterpart. Taking into account this greater diversity could help refine the curvature correction in eqn (27). In particular, for large curvature other polygonal shapes besides the pentagon could be relevant for disordered systems.

6 Discussion

Utilizing a mean field model we showed that the asymmetry of the linear response of the vertex model under dilation and compression extends away from the critical shape index for finite strains. The asymmetry reflects how an initially rigid tissue may be sufficiently compressed to induce shape degeneracy and thereby relax perimeter tension, yielding a softer bulk

modulus. Conversely, sufficient dilation applied to a compatible (floppy) cell lifts shape degeneracy, yielding an increase of the bulk modulus. Thus applied dilation and compression shift the rigidity of the VM in 2D.

Using this insight, we extend our mean field theory to calculate the effective dilation/compression engendered by intrinsic curvature and predict the curvature-induced shift of the rigidity transition by calculating the effective critical shape index. We compare our result to simulations by[15] and find good agreement.

Our mean field prediction provides a metric which can be applied to studying the rigidity transition in curved biological tissues in a manner analogous to studies in the flat case. Additionally, the shift of rigidity upon compression/dilation could be tested, for instance, in experiments such as those of ref. 22, where an epithelial monolayer is compressed or stretched *via* an underlying deformable substrate.

During the preparation of this manuscript, the authors became aware of a recent manuscript by ref. 23 which further verifies the role of curvature in the rigidity transition of the vertex model and also provides a complementary mean field theory on the rigidity transition.

Conflicts of interest

There are no conflicts to declare.

Appendices

A Appendix

A.1 Details about metric expansion

The purpose of this appendix is to give a brief explanation of the series expansion of the metric in terms of curvature. A complete and rigorous treatment may be found in many textbooks on Riemannian geometry such as in ref. 24–26. The metric is a second order symmetric tensor whose components are spatially dependent function of the surface. It governs all geometric data in that the distance between any two points is given by the line element

$$\mathrm{d}s^2 = g_{ij}(x)\mathrm{d}x^i\mathrm{d}x^j. \tag{28}$$

In general, about a given point $x_0 \in M$ the components of the metric may be approximated as constants to 1st order. One may diagonalize this approximation such that the metric at x_0 is given by δ_{ij}. However, expanding to 2nd order the metric's components are not necessarily also constant. In fact, if there exist coordinates such that the metric's expansion is constant up to 2nd order then the metric is totally flat in the neighborhood, which we will briefly show below. Normal coordinates about a point x_0 are defined as coordinates which parametrize a geodesic curve, γ^i, as a straight line, *i.e.* local coordinates x^i such that $\gamma^i(\lambda) = x^i\lambda$, where $\gamma(0) \equiv x_0$. In these coordinates the Christoffel symbols are extracted from the geodesic equation

$$0 = \frac{\mathrm{d}^2\gamma^i}{\mathrm{d}\lambda^2} + \Gamma^i_{k\ell}\frac{\mathrm{d}\gamma^k}{\mathrm{d}\lambda}\frac{\mathrm{d}\gamma^\ell}{\mathrm{d}\lambda}. \tag{29}$$

Utilizing normal coordinates, eqn (29) implies $\Gamma^i_{k\ell}(x_0) = 0$. Differentiation also yields the differential constraint equation.

$$\partial_j\Gamma^i_{k\ell}(x_0) + \partial_k\Gamma^i_{\ell j}(x_0) + \partial_\ell\Gamma^i_{jk}(x_0) = 0 \tag{30}$$

The Riemann curvature tensor is defined as

$$R^i_{jkl} = \partial_k\Gamma^i_{jl} - \partial_l\Gamma^i_{jk} + \Gamma^i_{pk}\Gamma^p_{kl} + \Gamma^{\mathrm{i}}_{pl}\Gamma^p_{kj}. \tag{31}$$

From the differential constraint and the definition of R^i_{jkl}, one can show

$$\partial_l\Gamma^k_{ij} = -\frac{1}{3}\left(R^k_{ijl} + R^k_{jil}\right). \tag{32}$$

Symmetry of the metric implies the covariant derivative of the metric vanishes, *i.e.* $\nabla\mathbf{g} = 0\partial_k g_{ij} - \Gamma^p_{jk}g_{ip} - \Gamma^p_{ik}g_{jp} = 0$. The second derivative of the metric in normal coordinates is

$$\partial_{kl}{}^2 g_{ij} = -\frac{1}{3}\left(R_{klij} + R_{jlik}\right). \tag{33}$$

The Taylor expansion of the metric in normal coordinates yields

$$g_{ij} = \delta_{ij} - \frac{1}{3}R_{ijk\ell}x^k x^\ell + \mathcal{O}(|x|^2). \tag{34}$$

Higher order terms can be generated iteratively by calculating higher order differential constraint equations from eqn (30) and $\nabla\mathbf{g} = 0$. For 2D surfaces the Riemann curvature tensor only has a single d.o.f. and admits the representation[25]

$$R_{iklj} = \mathcal{G}(g_{ik}g_{lj} - g_{ij}g_{kl}). \tag{35}$$

Where $\mathcal{G}$ is the Gaussian curvature. From this the Ricci tensor follows $R_{ij} \equiv g^{kl}R_{iklj} = \mathcal{G}g_{ij}$. Using the expansion of the metric, we have to lowest order

$$R_{iklj} = \mathcal{G}\left(\delta_{ik}\delta_{lj} - \delta_{ij}\delta_{kl}\right) + \mathcal{O}(|x|^2) \tag{36}$$

$$R_{ij} = \mathcal{G}\delta_{ij} + \mathcal{O}(|x|^2) \tag{37}$$

These expressions reflect that locally any surface looks either flat ($\mathcal{G} = 0$), spherical ($\mathcal{G} > 0$), or saddle-like ($\mathcal{G} < 0$). To lowest order the metric expansion about p becomes

$$g_{ij} = \delta_{ij} - \frac{1}{3}\mathcal{G}(\delta_{ik}\delta_{lj} - \delta_{ij}\delta_{kl})x^k x^l + \mathcal{O}(|x|^3) \tag{38}$$

and determinant yields

$$\det(g) = 1 - \frac{1}{3}\mathcal{G}|x|^2 + \mathcal{O}(|x|^3) \tag{39}$$

which shows how curvature induces local compression or dilation. Higher order terms contain gradients and higher order invariants of R_{ijkl}, and are completely determined by $\mathcal{G}$. It follows that if the quadratic contribution vanishes, then the metric is totally flat locally.

A.2 Perturbative polygon area expansion

To explicitly parameterize the polygonal cell D, we will consider a regular n-gon and decompose it into $2n$-triangles about its centroid as pictured in Fig. 4. Working in terms of polar coordinates, this yields for the first term

$$\begin{aligned}\int_D \mathrm{d}^2x &= 2n\int_0^{\frac{\pi}{n}}\int_0^{R_{\mathrm{cell}}\cos\left(\frac{\pi}{n}\right)\sec\theta} \mathrm{d}\theta r\,\mathrm{d}r \\ &= n{R_{\mathrm{cell}}}^2\cos\left(\frac{\pi}{n}\right)^2\tan\left(\frac{\pi}{n}\right)\end{aligned} \tag{40}$$

In the limit of $n \to \infty$ we get $\pi{R_{\mathrm{cell}}}^2$, as expected for circles. Using the same coordinate system, we compute the first correction due to curvature

$$\begin{aligned}\frac{\mathcal{G}}{6}\int_D |x|^2\mathrm{d}^2x &= \frac{\mathcal{G}}{6}2n\int_0^{\frac{\pi}{n}}\int_0^{R_{\mathrm{cell}}\cos\left(\frac{\pi}{n}\right)\sec\theta} \mathrm{d}\theta r^3\mathrm{d}r \\ &= \frac{\mathcal{G}}{12}{R_{\mathrm{cell}}}^4\cos^4\left(\frac{\pi}{n}\right)n\left(\frac{2}{3}+\frac{1}{3}\sec^2\left(\frac{\pi}{n}\right)\right)\tan\left(\frac{\pi}{n}\right)\end{aligned} \tag{41}$$

A.3 Mean-field vertex model

The mean field model is defined by the area and perimeter of a single cell, which is parameterized by n-edges ν_α given by

$$\vec{\nu}_\alpha \equiv \ell_0\left(\cos\left(\frac{2\pi\alpha}{n}\right),\sin\left(\frac{2\pi\alpha}{n}\right)\right) \tag{42}$$

where ℓ_0 the characteristic cell edge length. The perimeter is the sum of each edge length

$$P = \sum_\alpha^n \sqrt{\vec{\nu}_\alpha\cdot\vec{\nu}_\alpha} \tag{43}$$

Under an affine transformation, denoted as the matrix $\mathbf{F}$, the deformed perimeter is given by

$$P = \sum_\alpha^n \sqrt{(\mathbf{F}\vec{\nu}_\alpha)\cdot(\mathbf{F}\vec{\nu}_\alpha)}. \tag{44}$$

The area can be calculated by the cross product

$$A = \int_D \mathrm{d}x^2 = n|\vec{a}\times\vec{b}| \tag{45}$$

where $\vec{a}$ and $\vec{b}$ are defined in Fig. 4.

The deformed are is straightforward to calculate by using the identity $|(\mathbf{F}\vec{a})\times(\mathbf{F}\vec{b})| = \det(\mathbf{F})|\vec{a}\times\vec{b}|$. Thus under an affine transformation the deformed area can be written as

$$A = \det(\mathbf{F})n|\vec{a}\times\vec{b}| \tag{46}$$

$$= \det(\mathbf{F})\frac{n}{4}{\ell_0}^2\cot\left(\frac{\pi}{n}\right). \tag{47}$$

The energy per cell is cast as

$$\begin{aligned}E &= \frac{\kappa_A}{2}\left(\frac{n}{4}{\ell_0}^2\cot\left(\frac{\pi}{n}\right)\det(\mathbf{F})-A_0\right)^2 \\ &+ \frac{\kappa_P}{2}\left(\sum_\alpha^n\sqrt{(\mathbf{F}\vec{\nu}_\alpha)\cdot(\mathbf{F}\vec{\nu}_\alpha)}-P_0\right)^2\end{aligned} \tag{48}$$

To non-dimensionalize we define reference lengths ℓ_A and ℓ_P such that

$$A_0 = \frac{n}{4}\ell_A^2\cot\left(\frac{\pi}{n}\right) \tag{49}$$

$$P_0 = n\ell_P \tag{50}$$

And rescale energy by $\kappa_A{A_0}^2$, yielding

$$E = \frac{1}{2}\left(\ell^2\det(\mathbf{F})-1\right)^2+\frac{r}{2}\left(\ell\sum_\alpha^n\sqrt{(\mathbf{F}\vec{\nu}_\alpha)\cdot(\mathbf{F}\vec{\nu}_\alpha)}-s_0\right)^2 \tag{51}$$

where $r\equiv\frac{\kappa_P}{\kappa_A A_0}$, $s_0\equiv\frac{P_0}{\sqrt{A_0}}$ is the target shape index, and $\ell\equiv\frac{\ell_0}{\sqrt{A_0}}$ is the re-scaled characteristic cell edge length. In the incompatible state, the ground state corresponds to a regular polygon with ℓ_0 defined to minimize the energy. This involves solving the cubic equation defined $\frac{\partial E}{\partial\ell}=0$. The relevant solution obeys the inequality $\ell \le 1$ for all $s_0 \le s_0^*$. In the compatible state energy minimization yields $\ell \equiv 1$ for choices of r and $s_0 \ge s_0^*$.

A.4 Inputting deformations

We model all cell shape distortions due to both applied deformations and cell response of the cell by linear affine transformation $\mathbf{F}$. For example, compression/dilation correspond to

$$\mathbf{F}_\varepsilon = \begin{pmatrix}1+\varepsilon & 0\\ 0 & 1+\varepsilon\end{pmatrix}. \tag{52}$$

We also parametrize a self-shear corresponding to the cell adjusting its perimeter without changing the imposed re-scaled area by enforcing the constraint $\det(\mathbf{F}^{\mathrm{cell}}) = 1$. This only fixes a single degree of freedom, leaving in principle three components of $\mathbf{F}_{\mathrm{cell}}$ free. For simplicity, we only consider the cell's response by tilting through a simple shear transformation

$$\mathbf{F}_\theta^{\mathrm{cell}} = \begin{pmatrix}1 & \tan(\theta)\\ 0 & 1\end{pmatrix} \tag{53}$$

We set the overall transformation in the mean field model as

$$\mathbf{F} = \mathbf{F}_\theta^{\mathrm{cell}}\cdot\mathbf{F}_\varepsilon = (1+\varepsilon)\begin{pmatrix}1 & \tan(\theta)\\ 0 & 1\end{pmatrix} \tag{54}$$

Acknowledgements

A. H. thanks Mark Bowick for critical reading of the manuscript, helpful discussions and advice, as well as Fridtjof Brauns and Fernando Caballero for illuminating discussions. The authors also thank Daniel Sussman for sharing simulation data from ref. 15. A. H. and M. C. M. were supported by the US National Science Foundation Grant No. DMR-2041459. M. M. acknowledges support from the Israel Science Foundation, Grant No. 1441/19.

Notes and references

1 J.-A. Park, J. H. Kim, D. Bi, J. A. Mitchel, N. T. Qazvini, K. Tantisira, C. Y. Park, M. McGill, S.-H. Kim and B. Gweon, *et al.*, *Nat. Mater.*, 2015, **14**, 1040–1048.
2 R. Farhadifar, Dynamics of cell packing and polar order in developing epithelia, Dissertation, Technische Universität Dresden, 2009.
3 A. Hernandez, M. F. Staddon, M. J. Bowick, M. C. Marchetti and M. Moshe, *Phys. Rev. E*, 2022, **105**, 064611.
4 J. Huang, J. O. Cochran, S. M. Fielding, M. C. Marchetti and D. Bi, *arXiv*, 2021, preprint, arXiv:2109.10374, DOI: **10.48550/arXiv.2109.10374**.
5 D. Bi, J. Lopez, J. M. Schwarz and M. L. Manning, *Nat. Phys.*, 2015, **11**, 1074–1079.
6 R. Osserman, *et al.*, *Bull. Am. Math. Soc.*, 1978, **84**, 1182–1238.
7 M. Moshe, M. J. Bowick and M. C. Marchetti, *Phys. Rev. Lett.*, 2018, **120**, 268105.
8 R. Farhadifar, J.-C. Röper, B. Aigouy, S. Eaton and F. Jülicher, *Curr. Biol.*, 2007, **17**, 2095–2104.
9 D. B. Staple, R. Farhadifar, J.-C. Röper, B. Aigouy, S. Eaton and F. Jülicher, *Eur. Phys. J. E*, 2010, **33**, 117–127.
10 N. Murisic, V. Hakim, I. G. Kevrekidis, S. Y. Shvartsman and B. Audoly, *Biophys. J.*, 2015, **109**, 154–163.
11 M. J. Hertaeg, S. M. Fielding and D. Bi, *arXiv*, 2022, preprint, arXiv.2211.15015, DOI: **10.48550/arXiv.2211.15015**.
12 B. Schamberger, R. Ziege, K. Anselme, M. Ben Amar, M. Bykowski, A. P. Castro, A. Cipitria, R. A. Coles, R. Dimova and M. Eder, *et al.*, *Adv. Mater.*, 2023, **35**, 2206110.
13 F.-L. Wen, *Phys. Rev. E*, 2022, **106**, 064403.
14 Y. Ogura, F.-L. Wen, M. M. Sami, T. Shibata and S. Hayashi, *Dev. Cell*, 2018, **46**, 162–172.
15 D. M. Sussman, *Phys. Rev. Res.*, 2020, **2**, 023417.
16 M. F. Staddon, A. Hernandez, M. J. Bowick, M. Moshe and M. C. Marchetti, *Soft Matter*, 2023, **19**, 3080–3091.
17 K. A. Brakke, *Exper. Math.*, 1992, **1**, 141–165.
18 X. Mao and T. C. Lubensky, *Ann. Rev. Condens. Matter Phys.*, 2018, **9**, 413–433.
19 I. Levin and E. Sharon, *Phys. Rev. Lett.*, 2016, **116**, 035502.
20 M. Arieli, E. Sharon and M. Moshe, *arXiv*, 2021, preprint, arXiv.2105.00751, DOI: **10.48550/arXiv.2105.00751**.
21 A. Gray and L. Vanhecke, *Acta Mathematica*, 1979, **142**, 157–198.
22 E. Frittoli, A. Palamidessi, F. Iannelli, F. Zanardi, S. Villa, L. Barzaghi, H. Abdo, V. Cancila, G. V. Beznoussenko and G. Della Chiara, *et al.*, *Nat. Mater.*, 2023, **22**, 644–655.
23 M. De Marzio, A. Das, J. J. Fredberg and D. Bi, *arXiv*, 2023, preprint, arXiv.2305.12667, DOI: **10.48550/arXiv.2305.12667**.
24 A. Gray, *Tubes*, Springer Science & Business Media, 2003, vol. 221.
25 T. Willmore, *Riemannian Geometry*, Oxford Science Publications, 1993.
26 O. Veblen and J. Whitehead, *Foundations of Differential Geometry*, Cambridge Press, 1932.